C. R. Physique 17 (2016) 533–542

Contents lists available at ScienceDirect

Comptes Rendus Physique

www.sciencedirect.com

Phononic crystals / Cristaux phononiques

Negative refraction and imaging of acoustic waves in a two-dimensional square chiral lattice structure

Réfraction négative et imagerie des ondes acoustiques dans une structure périodique chirale bidimensionnelle

Sheng-Dong Zhao, Yue-Sheng Wang *

Institute of Engineering Mechanics, Beijing Jiaotong University, Beijing 100044, China

ARTICLE INFO

Article history:
Available online 18 February 2016

Keywords:
Phononic crystal
Chiral lattice
Acoustic wave
Negative refraction
Imaging
Beam separation

Mots-clés :
Cristal phononique
Réseau chiral
Onde acoustique
Réfraction négative
Imagerie
Séparation de faisceaux

ABSTRACT

The negative refraction behavior and imaging effect for acoustic waves in a kind of two-dimensional square chiral lattice structure are studied in this paper. The unit cell of the proposed structure consists of four zigzag arms connected through a thin circular ring at the central part. The relation of the symmetry of the unit cell and the negative refraction phenomenon is investigated. Using the finite element method, we calculate the band structures and the equi-frequency surfaces of the system, and confirm the frequency range where the negative refraction is present. Due to the rotational symmetry of the unit cell, a phase difference is induced to the waves propagating from a point source through the structure to the other side. The phase difference is related to the width of the structure and the frequency of the source, so we can get a tunable deviated imaging. This kind of phenomenon is also demonstrated by the numerical simulation of two Gaussian beams that are symmetrical about the interface normal with the same incident angle, and the different negative refractive indexes are presented. Based on this special performance, a double-functional mirror-symmetrical slab is proposed for realizing acoustic focusing and beam separation.

RÉSUMÉ

La réfraction négative et l'imagerie des ondes acoustiques dans une structure périodique chirale bidimensionnelle sont étudiées dans cet article. La cellule élémentaire de la structure considérée comporte quatre bras en zigzag, connectés dans la partie centrale par un fin anneau circulaire. La relation entre la symétrie de la cellule élémentaire et le phénomène de réfraction négative est explorée. À l'aide de la méthode des éléments finis, nous calculons la structure de bande et les surfaces équifréquence du système, ce qui nous permet de confirmer la gamme de fréquence pour laquelle la réfraction négative est obtenue. En raison de la symétrie par rotation de la cellule élémentaire, une différence de phase est introduite pour les ondes émises par un point source et traversant la structure. Cette différence de phase est liée à la largeur de la structure ainsi qu'à la fréquence de

* Corresponding author.
E-mail address: yswang@bjtu.edu.cn (Y.-S. Wang).

http://dx.doi.org/10.1016/j.crhy.2016.02.003
1631-0705/

la source, ce qui nous permet d'obtenir une image défléchie avec un angle ajustable. Le même phénomène est également démontré par simulation numérique pour deux faisceaux gaussiens incidents, avec des angles symétriques par rapport à la normale à l'interface. Dans ce cas, différents indices de réfraction négatifs sont obtenus. Sur la base de ce comportement spécifique, une dalle présentant une symétrie miroir est proposée pour réaliser la double fonction de focalisation et de séparation de faisceaux acoustiques.

1. Introduction

Negative refractions of electromagnetic waves were theoretically predicted in the left-handed materials (LHMs) by Veselago in 1968 [1], but only recently were they demonstrated experimentally [2,3]. These materials are characterized by simultaneous negative permittivity and permeability [4–9]. LHMs possess a series of unusual electromagnetic effects, including negative index of refraction [1], inverse Snell's law [6,7], reversed Doppler shift [8], and reversed Cerenkov radiation [9]. Due to the unique physical properties and potential applications, left-handed materials with negative refraction have been a hot focus of interest. The focusing of electromagnetic waves using a flat lens was first proposed by Pendary and realized by Smith et al. [2,3]. There are two cases when one achieves negative refraction: the first case is the above-mentioned LHM having the simultaneous negative permittivity ε and negative permeability μ. In this case, $\boldsymbol{k}$, $\boldsymbol{E}$ and $\boldsymbol{H}$ form a left-handed set of vectors, i.e. $\boldsymbol{S}\cdot\boldsymbol{k} < 0$ (i.e. the pointing vector $\boldsymbol{S}$ and the wave vector $\boldsymbol{k}$ are in opposite directions). The other type is based on a photonic crystal (PtC) that has an effective refractive index controlled by the band structure [10,11], and the properties are similar to the right-handed medium, i.e. $\boldsymbol{S}\cdot\boldsymbol{k} > 0$. Therefore, the negative refraction can be realized without employing a negative index or a backward wave effect.

Very recently, these investigations in electromagnetic materials have been extended to acoustic and elastic media, and the acoustic and elastic LHMs have been proposed through phononic crystals (PnCs) by many researchers [12–18]. The negative refraction was realized by a metamaterial slab with simultaneously negative mass density and modulus [19–21]. Most of the studies were also devoted to PnCs with solid scatterers immersed in a fluid (liquid or air) matrix, in which only longitudinal waves propagate [16–18] and the negative refraction is observed at the lowest valence band. Single mode and high transmission are the advantages of the negative refraction in the lowest valence band. This negative index PnC can help us to break the diffraction limit and realize the focusing of the waves by a flat superlens [16]. The waves generated from a source include propagating waves and evanescent waves. These latter carry the subwavelength details of the source and can be amplified by the lens made of a negative index material; therefore, a subwavelength imaging is achieved. This kind of lens is expected to have significant applications such as coupling or integration with various types of acoustic devices. Ke et al. [22] studied two-dimensional (2D) phononic crystals made of stainless steel rods immersed in water and assembled in a triangular crystal lattice. Recently, Alexey Sukhovich et al. [16] experimentally studied this kind of structure and confirmed the existence of negative refraction phenomenon. They obtained negative refraction by employing circular equi-frequency surfaces (EFSs) in the second band. Liu et al. [23] extended the study of negative refraction imaging effect to a 2D three-component phononic crystal consisting of square arrays of coated cylinders in a liquid matrix. High-intensity-focused ultrasound is a new kind of noninvasive treatment technology. Therefore, achieving high-quality near-field medical imaging is significant. For this kind of applications, it seems necessary to consider a structure that can be easily handled; and it is more appropriate to consider a PnC slab made of a solid matrix rather than of a fluid one. As it is well known, negative refraction phenomena in PnCs made of solid matrices are more complex due to the coupling of the longitudinal and transverse waves [24–28]. Vasseur et al. [25] experimentally evidenced the negative refraction of longitudinal waves in a 2D PnC with a solid matrix. Hladky-Hennion et al. [28] theoretically and experimentally investigated a PnC slab made of a single metallic phase and displayed perfect negative index matching and focusing capability when surrounded with water. Very recently, Zhou et al. [29] studied the acoustic super focusing and imaging by a general isotropic solid acoustic metamaterial and discussed the influence of the shear modulus on the spatial focusing resolution. Addouche et al. [30] demonstrated super resolution imaging of surface acoustic waves using a phononic structure; and they also described an all-angle negative refraction effect of surface acoustic waves in two-dimensional phononic crystals [31].

As for chiral phononic crystals, Spadoni et al. [32] have investigated the dispersive properties of chiral-like systems; Zhu et al. [33] presented a solid chiral microstructure capable of achieving sub-wavelength negative refraction of elastic waves. In this paper, we propose a kind of square chiral lattice structure made by etching periodic vacuum holes in a homogeneous solid matrix. The superlens is surrounded with a biological fluid like water; and the water is just in contact with outside surfaces of the constructed slab [28]. To the best of our knowledge, most negative refraction images reported in the literature were implemented with square-symmetrical configurations. There are few reports on rotationally symmetrical (chiral) structures for focusing the acoustic waves. The lattice structure proposed in the present paper consists of four zigzag bending arms connected through a thin circular ring at the central part. Wang et al. [34] proposed several kinds of 2D square zigzag lattice structures and verified that the bending arms can depress the bands. We show in this paper that based on this feature, a flat band can be found in the low-frequency region and a M-centered EFS is indeed obtained. In

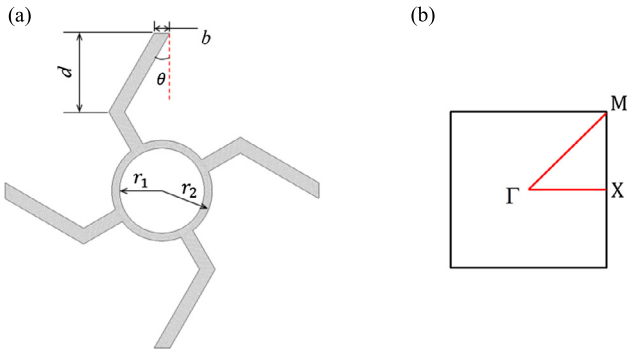

Fig. 1. (a) The unit cell of the proposed 2D square chiral lattice structure with four zigzag arms connected through a thin circular ring; and (b) the corresponding irreducible Brillouin zone.

this case, the lattice structures have an effective refractive index controlled by the band structure, and behave much like uniform right-handed medium, i.e. $\boldsymbol{S}\cdot\boldsymbol{k} > 0$.

2. Problem statement and computational model

We consider a 2D square zigzag lattice structure with the unit cell shown in Fig. 1a. The unit cell consists of four zigzag arms connected with a thin circular ring at the central part. Its geometry is characterized by five parameters presented in Fig. 1a. They are: the bending angle of the arms (θ), the horizontal (or vertical) thickness of the arms (b), the horizontal (or vertical) length of the arms (d), and the inner and outer radii of the circular ring (r_1, r_2). Assume that the lattice constant is a and $d = 0.25a$, then the porosity can be calculated as

$$f = \frac{a^2 - 2ab + 4br_2\cos\theta - \pi(r_2^2 - r_1^2)}{a^2} \tag{1}$$

Typically, when $\theta = 0°$, we have a square lattice structure with straight arms.

In this paper, the band structures, EFSs, and the negative refraction properties of the proposed structure will be studied. The calculation is based on the finite element method. The commercial software COMSOL is used and the unit cell is meshed by using a default triangular mesh with Lagrange quadratic elements provided by COMSOL. Bloch conditions are applied on the opposite boundaries of the unit cell, and traction-free conditions are applied on the other boundaries. The irreducible Brillouin zone is presented in Fig. 1b, and the dispersion relations are obtained by sweeping the wave vector along the edges of the irreducible Brillouin zone [34]. For the computation of the acoustic pressure field, the frequency response model is used and the plane wave radiation conditions are applied on the external boundaries of the water regions.

Next, we will present the detailed numerical results of the band structures and EFSs. The influences of the geometry on the negative refraction index and acoustic focusing effects will be analyzed. Particularly, we will reasonably discuss the design of a multi-functional slab based on the proposed structure.

The lattice structure is made of aluminum and surrounded by water. The properties of the aluminum are: the mass density $\rho = 2700$ kg/m^3, Young's modulus $E = 70.3$ GPa, and Poisson's ratio $\upsilon = 0.346$. For the water, the density is $\rho = 1000$ kg/m^3; the wave velocity is $c = 1490$ m/s. The reduced frequency $\Omega = \omega a/2\pi c$ is used in the band structures.

3. Asymmetry negative refraction

We first discuss the negative refraction phenomenon for various bending angles of the zigzag arms by fixing the other geometrical parameters as: $a = 2$ cm, $b = 0.05a = 0.1$ cm, $d = 0.25a = 0.5$ cm, $r_1 = 0.145a = 0.29$ cm and $r_2 = 0.16a = 0.32$ cm. In this case, if the bending angle θ varies from 10° to 45°, the corresponding porosity range of the lattice structure is from 0.908 to 0.918. The band structures for different bending angles of $\theta = 30°$, 0° and 45° are illustrated in Figs. 2a–d, respectively. It is shown that the negative refraction may occur around the reduced frequency $\Omega = 0.224$, with the bending angle $\theta = 30°$, see Fig. 2a. Because the useful single-mode for negative refraction imaging is around point M, the water line ($\omega = ck$) is plotted from this point. The bold horizontal line at the reduced frequency of 0.224 marks the reduced frequency at the intersection point of the 4th band and the dispersive curve of the water. It is noted that a complete bandgap appears between the 4th and 5th bands in Fig. 2a (shadowed area), and that a single-mode exists at the concerned reduced frequency of 0.224. To know the property of the mode at the intersection point, we define a longitudinal polarization as

$$m_{\mathrm{p}} = \frac{\int_S |u_{\mathrm{L}}|^2 \mathrm{d}S}{\int_S (|u_{\mathrm{L}}|^2 + |u_{\mathrm{S}}|^2)\mathrm{d}S} \tag{2}$$

with the integral taken over the whole unit cell S [35]. u_{L} and u_{S} are the co-existing polarization displacement components parallel and perpendicular to the wave vector, respectively. Obviously, when $m_{\mathrm{p}} = 1$, we have a purely longitudinal

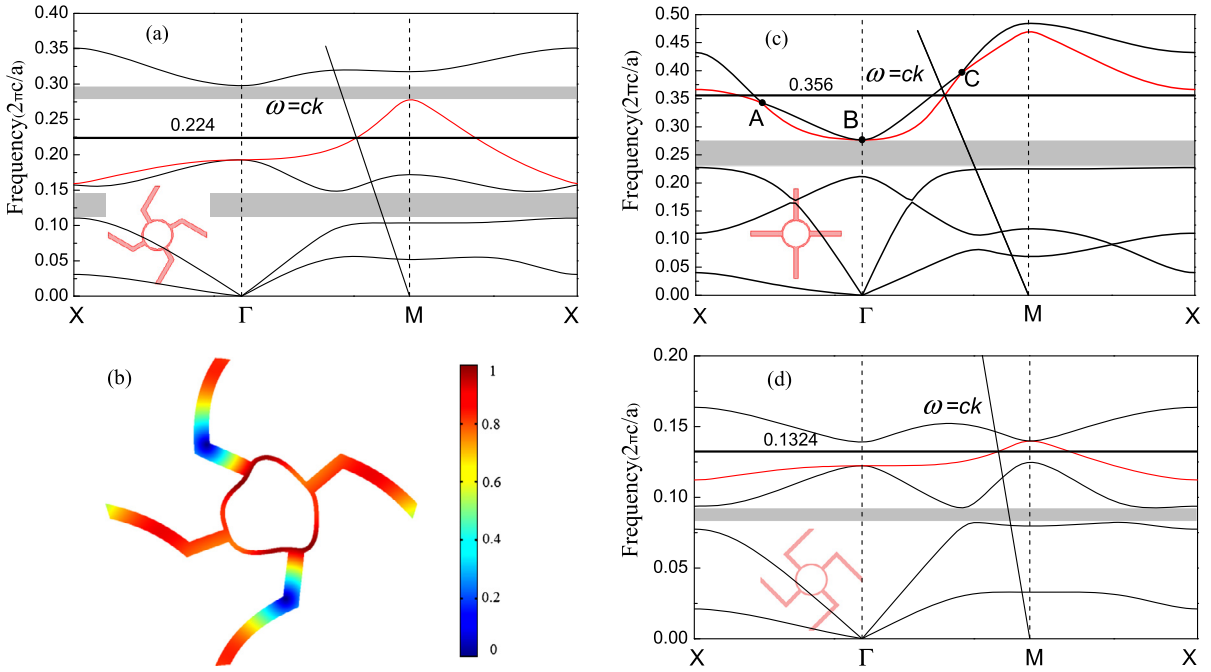

Fig. 2. The band structures for different bending angles of the zigzag arms: (a) $\theta = 30°$, (c) $\theta = 0°$ and (d) $\theta = 45°$. The other parameters are fixed as $a = 2$ cm, $b = 0.05a$, $d = 0.25a$, $r_1 = 0.145a$ and $r_2 = 0.16a$. The straight line, which is the dispersion curve in water ($\omega = ck$), intersects the negative branch (the 4th band) at the frequency marked by the bold horizontal line. (b) is the vibrational mode at the intersection point as shown in (a).

mode; when $m_p = 0$ we have a purely transverse mode. Because the intersection point locates at the Γ–M direction, the polarization of the longitudinal mode at this point should be along the Γ–M direction, with the polarization angle $\alpha = 45°$. Therefore, we have:

$$u_L = u\cos 45° + v\cos 45°,$$
$$u_S = -u\cos 45° + v\cos 45°$$

with u and v representing the horizontal and vertical displacement components, respectively. It is easily calculated that $m_p = 0.77$ at the intersection point, which means that this mode is dominantly longitudinally polarized (see the vibrational mode shown in Fig. 2b), and thus can be coupled with incident longitudinal waves when the lattice structure is sandwiched between the water regions. Based on the band structure, the EFSs (Fig. 3a) are calculated for the acoustic waves propagating from the water to the lattice structure with the interface normal along Γ–M direction. It is noted that $\boldsymbol{S}\cdot\boldsymbol{k} > 0$ at the 4th band, and therefore the group velocity is never opposite to the phase velocity. In this case, the negative refraction can be obtained with the incident and refracted waves standing on the same side of the interface normal.

The numerical tests show that the negative refraction is significantly influenced by the bending angle θ of the zigzag arms. The negative refraction phenomenon will occur only when the bending angle takes a proper value between 10° and 40°, that is, a very big (near 45°) or very small (near 0°) angle does not produce negative refraction. To demonstrate this property, we illustrate the band structures in Fig. 2 for three cases: the bending angle takes the minimum value (0°), the maximum value (45°), and a medium value (30°). It is shown in Fig. 2c that a complete bandgap appears between the 3th and 4th bands (shadowed area) instead of the 4th and 5th bands in the case of straight arms ($\theta = 0°$). There are three degeneracy points marked by A, B and C between the 4th and 5th bands in Fig. 2c. In other words, different modes are coupled together at the crossover region; and a single mode does not exist at the reduced frequency of 0.356 marked by the horizontal line anymore. Meanwhile, the convex contour of EFS at this frequency disappears because the horizontal line only has one intersection point with the 4th band around point M. The band structures are depressed when the bending angle increases to $\theta = 45°$; and a single mode exists at the reduced frequency of 0.1327, marked by the horizontal line, see Fig. 2d. The properties of the band structures are similar to those with $\theta = 30°$. However, the symmetry of the wave-vector space is decreased extremely and the distortional EFSs occur (see Fig. 3b). As a result, the negative refraction vanishes.

The above results demonstrate that the negative refraction is obtained when $\theta = 30°$. As we know, the negative refraction is of help in realizing the imaging by a flat lens [28]. However, the imaging feature of a rotational symmetric structure is different from that of a square-symmetric structure. For the latter case, all the waves generated from a point source will be focused to a point image located at the Γ–M direction by a flat lens. But the rotational symmetry of the unit cell will lead to a rotational wave vector ($\boldsymbol{k}$) space (an increasing θ in Fig. 1a will make the EFS rotate clockwise). And thus the incident waves that are symmetrical about the interface normal will be refracted in different angles. From Fig. 3a, we can see that the

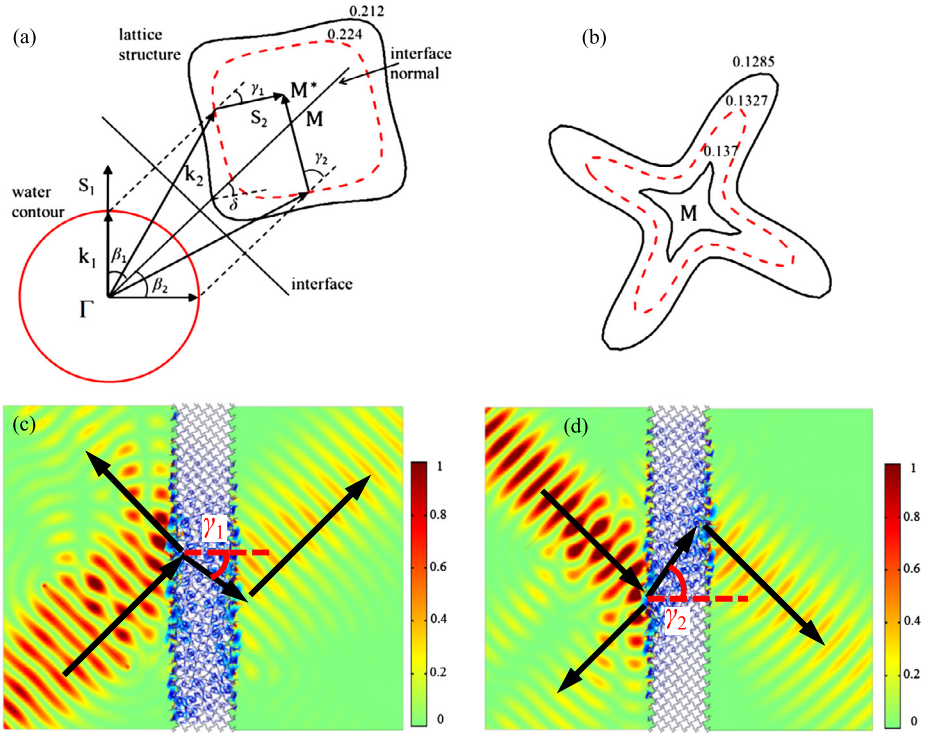

Fig. 3. (a) The EFSs of two frequencies at the 4th band for $\theta = 30°$. The red solid and dashed curves are for the EFSs of water and of the lattice structure at the reduced frequency of 0.224, respectively. Two incident waves with $\beta_1 = \beta_2 = 45°$ are focused on point M* rather than on point M, and the corresponding negative refraction angles are $\gamma_1 = -35.7°$ and $\gamma_2 = -55.7°$. The normally incident wave with refracted angle $\delta = 32.2°$ at the reduced frequency of 0.212 is also presented. (b) The EFSs of some frequencies around the intersection point at the 4th band when $\theta = 45°$. (c) and (d) are, respectively, the numerical simulation of two Gaussian beams incident to a 11-layered lattice slab in symmetrical directions (about the interface normal) with $\beta_1 = \beta_2 = 45°$.

Table 1
Relations between the bending angle θ and the negative refractive angles (γ_1, γ_2) as well as the reduced frequency Ω at the intersection point.

θ	10°	11°	12°	13°	14°	15°	20°	25°	30°	35°	36°	37°	38°	39°	40°
Ω	0.32	0.316	0.312	0.308	0.304	0.299	0.277	0.252	0.224	0.196	0.189	0.183	0.177	0.171	0.165
γ_1	21.7°	23.7°	27.3°	29.1°	31.4°	34.3°	36.6°	34.5°	35.7°	30°	31.7°	30.5°	28.7°	27°	21.5°
γ_2	52.3°	53.4°	56.2°	57.7°	58.5°	59.9°	60.4°	58°	55.7°	57.1°	57.1°	57.2°	57.6°	58.3°	58.9°
$\gamma_1 + \gamma_2$	74°	77.1°	83.5°	86.8°	89.9°	94.2°	97°	92.5°	91.4°	87.1°	88.8°	87.7°	86.3°	85.3°	80.4°

two incident waves with $\beta_1 = \beta_2 = 45°$ are focused to point M* rather than point M. The corresponding negative refraction angles are $\gamma_1 = -35.7°$ and $\gamma_2 = -55.7°$, respectively. According to the Snell's law, the relevant effective refractive indexes (with respect to the refractive index of the water) are $n_1 = -1.21$ and $n_2 = -0.86$, respectively. The phenomenon is also demonstrated by the numerical simulation of two Gaussian beams that are symmetrical about the interface normal with the same incidence angle of 45° (see Figs. 3c and 3d). The refractive angles can be indeed approximately evaluated as $\gamma_1 \approx -35.7°$ and $\gamma_2 \approx -55.7°$, respectively, which is in good agreement with the above prediction. In addition, the reflected waves occur due to a large mismatch between the lattice structure and the water.

Fig. 3a shows that the EFS (the red dashed curve) is approximately a square. Therefore, the negative refraction angles γ_1 and γ_2 will not change in a discernible fashion when the incident angles β_1 and β_2 vary in a relatively wide range. Specifically, when the incident angle β_1 is between $17.3° \sim 47.5°$ and β_2 between $33.1° \sim 63.1°$, the refraction angle will not deviate by 3°.

Next we check the influence of the bending angles on the negative refraction phenomenon. The negative refractive angles (γ_1, γ_2) and the corresponding frequency (Ω) marked by the horizontal line under different bending angles (θ) are listed in Table 1. It can be seen that when the bending angle θ increases from 10° to 40°, the reduced frequency (Ω) decreases from 0.32 to 0.165. This verifies that the bending arms can depress the band structure. It is interesting to notice that γ_1 increases with the bending angle increasing from 10° to 15° and then remains relatively stable around 35° when θ varies in the range of $15° \sim 30°$. When the bending angle further increases, the refraction angle γ_1 decreases again. On the other hand, the variation of the refraction angle γ_2 with the bending angle θ is much more complex. However, it can be noticed that the sum of the two refraction angles $(\gamma_1 + \gamma_2)$ remains around 90° when the bending angle varies from 14° to 37°.

Table 2
Relations between the different inner r_1 and the negative refractive angles (γ_1, γ_2) as well as the reduced frequency Ω at the intersection point.

r_1 (cm)	0.28	0.285	0.29	0.295	0.3	0.305
$r_2 - r_1$ (cm)	0.04	0.035	0.03	0.025	0.02	0.015
Ω	0.245	0.236	0.224	0.209	0.19	0.162
γ_1	15.9°	29.2°	35.7°	39.7°	40.7°	37.5°
γ_2	68.8°	61.9°	55.7°	53°	50°	46°
$\gamma_1 + \gamma_2$	84.7°	91.4°	91.4°	92.7°	90.7°	83.5°

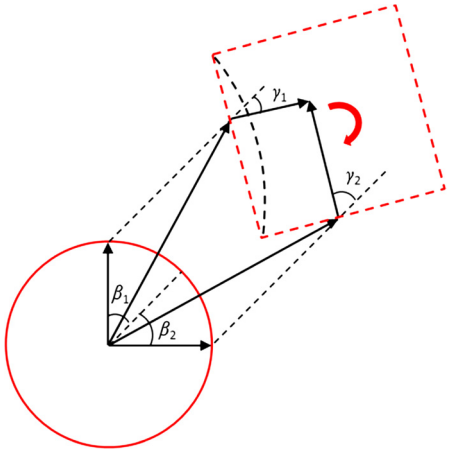

Fig. 4. Schematic diagram for the negative refraction waves with incident angles of $\beta_1 = \beta_2 = 45°$. The red square dashed curve is for the EFS of the negative refraction frequency under ideal conditions, and the black dashed curve shows the distortion of the EFS.

The circular ring thickness $(r_2 - r_1)$ can also influence the negative refraction phenomenon significantly. Next we discuss the influence of the inner radius r_1 on the reduced frequency (Ω) marked by the horizontal line and the negative refraction angles (γ_1, γ_2) for the bending angle $\theta = 30°$ with the other parameters being fixed as above. The results are listed in Table 2 for the inner radius r_1 varying from 0.28 cm to 0.305 cm, i.e. the thickness $(r_2 - r_1)$ decreasing from 0.04 cm to 0.015 cm. The table shows that a thinner circular ring yields a lower eigenfrequency and a smaller negative refraction angle γ_2. But γ_1 first increases and then decreases with the thickness decreasing. Anyhow, the sum of γ_1 and γ_2 keeps stably around 90° when r_1 ranges from 0.285 cm to 0.3 cm.

Fig. 3a demonstrates that when the negative refraction happens, the corresponding EFS is similar to a square (see the red dashed curve in Fig. 3a). With the bending angle θ increasing, the EFS rotates clockwise and is distorted gradually. Ideally, the EFS is a square when perfect negative refraction happens as shown schematically by the red dashed curve in Fig. 4. The distortion of the EFS is shown by the black dashed curve. The refraction angle γ_1 is determined by the rotation and distortion of the EFS simultaneously. It increases with the rotation proportionally, but decreases with the distortion in a complex nonlinear manner. So when the rotation acts as a major role, γ_1 increases with θ increasing $(\theta < 15°)$. But when the distortion acts as a major role, γ_1 decreases with θ increasing $(\theta > 30°)$. The refraction angle γ_1 keeps relatively stable when the effects of the two roles are comparable $(15° < \theta < 30°)$. It can be understood that $\gamma_1 + \gamma_2 = 90°$ under the ideal condition (Fig. 4). Therefore, in practice, the values of θ corresponding to $\gamma_1 + \gamma_2 \approx 90°$ are termed effective bending angles. From Table 1, we find that the effective bending angle for the present case is between 14° and 37°.

With the inner radius r_1 increasing, the ring stiffness decreases and yields a lower eigenfrequency. The circular ring at the central part can resist the rotational trend of $\boldsymbol{k}$ space. A decrease in the ring stiffness results in a rotation of the EFS, with gradual distortion. Thus with r_1 increasing, γ_1 first increases and then decreases (similar to the variation of γ_1 with θ). The range of the effective radius r_1 corresponding to $\gamma_1 + \gamma_2 \approx 90°$ is 0.285 cm $< r_1 <$ 0.3 cm.

4. The deviated imaging

It is known that focusing and imaging of acoustic waves through a PnC slab may be realized by taking advantage of negative refraction. Because of the rotational properties of the present structure, a phase difference is induced to the incident waves generated from a point source, and a deviated imaging point may be obtained, i.e. the image does not lie right ahead of the source point. Next, we will examine the relationship of the phase difference with the lens width and the source frequency. The black solid arrows in Fig. 5a schematically show how the acoustic waves propagate through the lattice slab composed of chiral unit cells with negative refraction index and how the deviated image is obtained by the slab (with $\theta = 30°$ and $r_1 = 0.29$ cm). We particularly present the intensity distribution of the pressure fields with imaging effects. Two slabs with 14 and 9 layers of chiral cells are shown in Figs. 5b and 5c, respectively. The source points are placed on

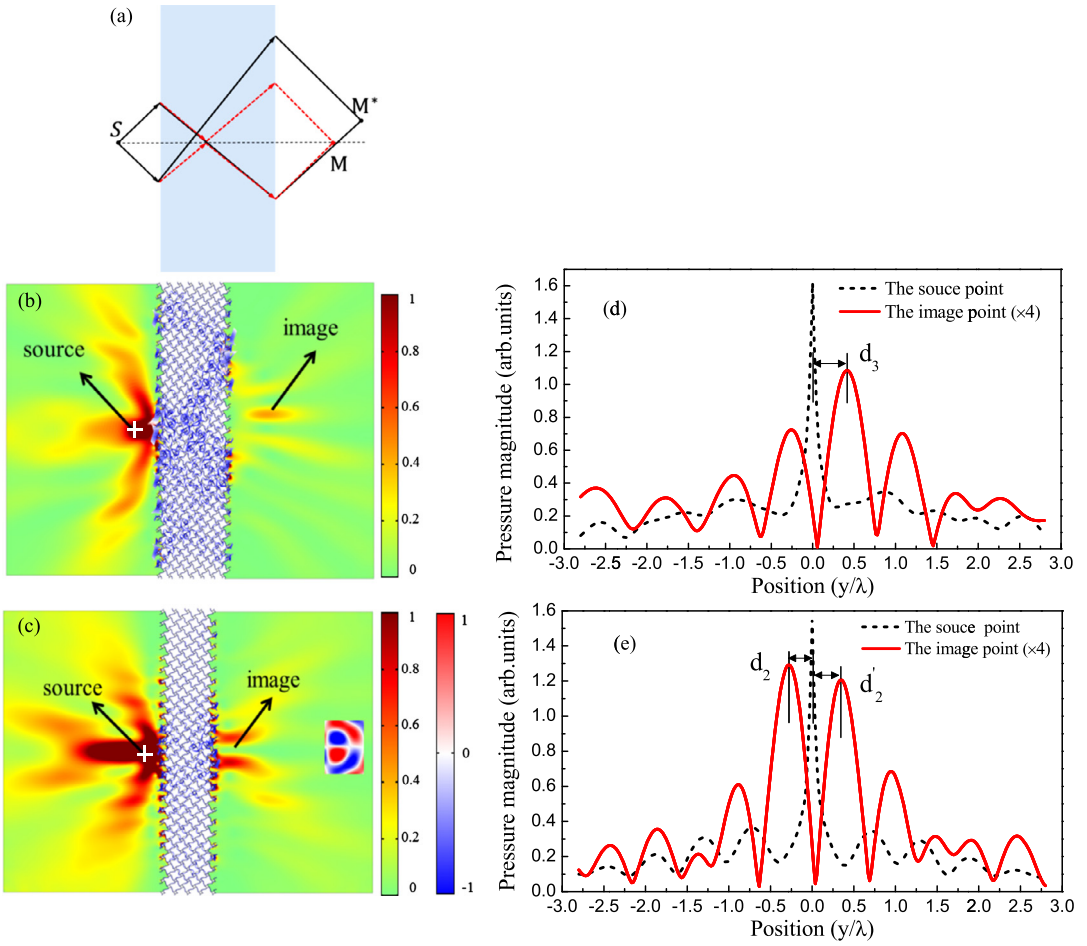

Fig. 5. (a) Schematic diagram for a point source of acoustic waves through a slab with the surface normal in the Γ–M direction. The black solid arrows schematically show how the acoustic waves propagate through the lattice slab composed of chiral unit cells with negative refraction index, while the red dashed arrows represent the propagation path for a mirror-symmetrical slab. (b) and (c) show the imaging effects of two slabs with 14 and 9 layers of unit cells. The source is marked by a white cross. (d) and (e) present the pressure magnitude distributions of the source and image points corresponding to (b) and (c), respectively.

the left side of the slab (the distance to the left interface is $2a$) with the excitation reduced frequency of 0.224. It is seen from Fig. 5b that the acoustic waves are focused to a point with a deviated distance $d_3 = 0.45\lambda$ (see the pressure amplitude distribution shown in Fig. 5d). However, for the thinner slab with 9 layers shown in Fig. 5c, the negative refracted waves are focused to two points and their distances to the central line are almost the same, i.e. $d_2 \approx d_2' = 0.34\lambda$, see the pressure amplitude distribution shown in Fig. 5e. Moreover, the phases of the two points are opposite, see the inset of Fig. 5c. This anomalous result is induced by the intense phase difference (nearly opposite) of the focused waves that cannot be coupled into one point image. Both images in Figs. 5b and 5c obey the wave-beam negative refraction law, but are obviously different because the phase difference is significantly influenced by the slab width. A similar conclusion can also be obtained if the frequency of the source is changed, the slab thickness remaining unchanged.

5. A double-functional mirror symmetry slab

A multi-functional slab has attractive application prospects in the field of designing acoustic devices. In this part, we design a 14-layered mirror-symmetrical slab (MSS) whose two parts are symmetric with respect to the line at the central part (see Fig. 6a). The other geometrical parameters are fixed as the first example in Section 3. The MSS is sandwiched by water areas which are marked with A and B. In our model, the source point is placed on the symmetrical line (see Fig. 6a) in the left part A and its distance to the left interface (between the water and the slab) is $2a$. The refracted waves generated from the point source are symmetric, so the phase difference can be eliminated and the outgoing waves are focused on the symmetrical line in part B, as shown in Fig. 6c. To demonstrate how the acoustic waves propagate through the MSS, we refer to the schematic diagram of Fig. 5a, where the red dashed arrows illustrate the wave propagation path in the MSS and the black dashed line represents the symmetrical line, i.e. the interface between the two parts of the slab. The waves at the

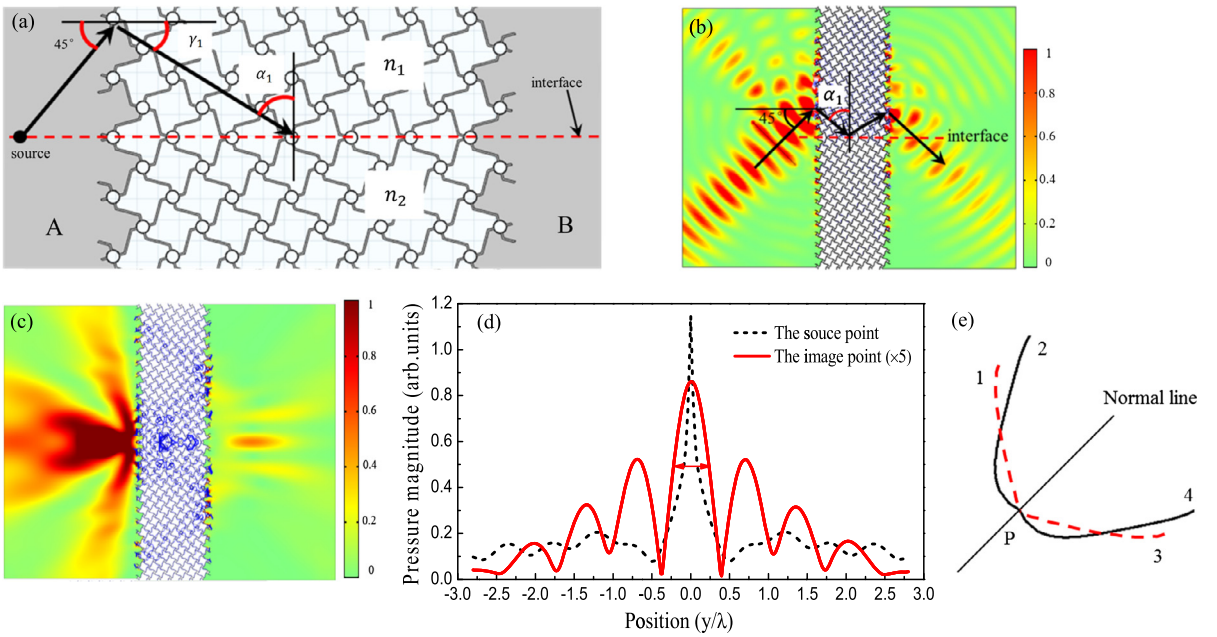

Fig. 6. (a) The 14-layered mirror-symmetrical slab (MSS), which is sandwiched by water areas marked by A and B. (b) Numerical simulation of the total reflection for a wave beam. (c) Numerical simulation of the imaging effect of a source point in part A at the reduced frequency of 0.224. (d) Pressure magnitude distribution of the source and image points. The red arrow shows the full width at half maximum of the transmission peak measured at the basis of the peak. (e) The mirror-symmetrical EFSs for the waves generated from the sources in the two parts of A and B.

interface between the symmetric two parts follow Snell's law, and the total reflection may take place when $|n_1| > |n_2|$ as shown in Fig. 6a. We can calculate the critical angle α_c for total reflection through

$$\sin\alpha_c = n_2/n_1$$

We recall that $n_1 = -1.21$ and $n_2 = -0.86$, which are given in Section 3. Then the critical angle is $\alpha_c = 45.3°$. The incidence angle α_1 (as shown in Fig. 6a) is

$$\alpha_1 = 90° - |\gamma_1|$$

Section 3 presents the result of $\gamma_1 = -35.7°$, then we have $\alpha_1 = 54.3°$.

When $\alpha_1 > \alpha_c$, the total reflection will take place at the interface. The corresponding numerical simulation is shown in Fig. 6b. From Fig. 6c, we can know that all the totally reflected waves are focused to a spot at part B. If we use a thicker slab, the imaging spot will be more far away from the right boundary of the slab.

The pressure amplitude distribution of the source and image points along the vertical direction (y axis) is plotted in Fig. 6d for comparison, and we can find that the pressure level at the image point is about 15% of the pressure level at the source point. The result also clearly demonstrates the sub-diffraction-limited acoustic focusing with a spatial resolution of 0.49λ, which is defined as the full width at half maximum of the transmission peak measured at the basis of the peak [16]. More importantly, the negative refraction effect is irreversible. That is, if the source point is set at part B, the focusing effect at part A is worse. This irreversible wave phenomenon is caused by the mirror symmetry of the slab. The wave incident to the upper part of the MSS is refracted at the same angle with the incident wave to the lower part. This is understood by considering the mirror symmetry of the EFSs, see Fig. 6e, where curve 1 and curve 4 represent parts of the original EFS for the unit cell as shown by the red dashed curve in Fig. 3a. For the mirror-symmetrical slab, the EFSs for the incident waves are symmetrical about the normal line in Fig. 6e. The red dashed curve (composed of curves 1 and 3) is the mirror-symmetrical EFS for the waves generated from the source at part A, while the black solid curve (composed of curves 2 and 4) is the mirror-symmetrical EFS for the source at part B. Fig. 6e shows that the red dashed curve is more propitious to focus the refracted waves on account of its convex property, while that the black solid curve has a concave character at point P, which is a disadvantage for the imaging effect.

Interestingly, another function—the beam separation—can also be realized by this MSS. In the rotationally symmetrical slab proposed in the previous Section 4, the normally incident wave will be refracted and deviated from the original propagation direction. For instance, from the EFS for the reduced frequency of 0.212 shown in Fig. 3a, we can observe that the refracted angle for the normally incident wave is $\delta \approx 32°$. Fig. 7a demonstrates a normally incident Gaussian beam passing through the slab. The outgoing beam deviates from the original direction. From this result, we can know that an incident Gaussian beam from part B passing through the MSS along the symmetrical axis is equally divided into two beams, see

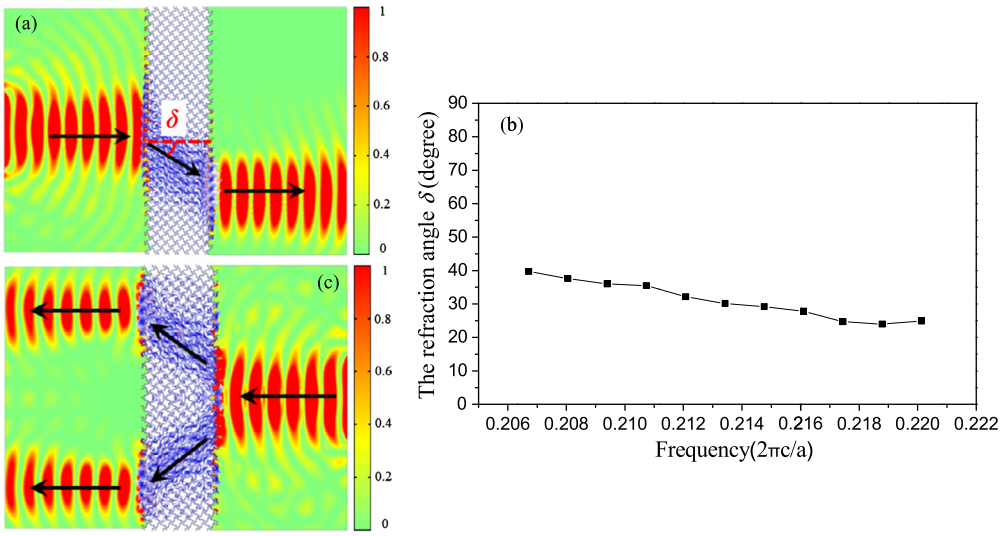

Fig. 7. (a) Numerical simulation for the normal incidence of waves into the rotationally symmetrical slab proposed in Section 4 at the reduced frequency of 0.212. (b) Relationship of the united frequency and its corresponding refraction angle δ. (c) Numerical simulation of the beam separation phenomenon at the reduced frequency of 0.212. The Gaussian beam is normally incident to the MSS from part B and will be equally divided into two beams in part A.

Fig. 7b. The effective beam separation frequency range is also a significant consideration. It is easily checked that the proposed MSS can realize beam separation in a relatively wide frequency range of 0.206 to 0.22. However, the separation angle δ only can be controlled in a relatively narrow range and is not related to the thickness of the slab, as shown in Fig. 7c.

6. Conclusions

In this paper, we have proposed a kind of 2D square chiral lattice structure of which the unit cell consists of four zigzag arms connected through a thin circular ring at the central part. Using the finite element method, we calculate the band structures and the EFSs of the considered system, thereby verifying the existence of the negative refraction. The effects of the geometric parameters, the bending angle of the arms and the ring thickness on the negative refraction are discussed. The imaging property of a chiral slab is also examined. Then we propose a mirror-symmetrical slab and research its multiple functions—imaging and beam separation. The following conclusions can be drawn.

1. A chiral unit cell with rotational symmetry will lead to a rotational wave vector ($\boldsymbol{k}$) space. Two incident wave beams that are symmetrical about the interface normal will be refracted in different angles. With the bending angle of the zigzag arms increasing, the EFS rotates clockwise and is distorted gradually. The refraction angle is determined by the rotation and distortion of the EFS simultaneously.
2. The circular ring at the central part can resist the rotational trend of $\boldsymbol{k}$ space. With the circular ring thickness decreasing, the ring stiffness decreases and results in rotation of the EFS, with gradual distortion.
3. Under some values of the bending angle and circular ring thickness, which are termed effective bending angles and ring thicknesses, the sum of the two refraction angles ($\gamma_1 + \gamma_2$) for the two incident wave beams symmetrical about the interface normal remains around 90°.
4. The negative refractive imaging is significantly influenced by the slab width. One-deviated-point imaging or two-point imaging can be realized depending on the slab's width.
5. For the mirror-symmetrical slab, the refracted waves generated from a point source at one side of the slab are symmetric, and therefore the phase difference can be eliminated and the outgoing waves are focused on the symmetrical line at the other side of the slab. In addition, an incident Gaussian beam with a relatively wide frequency range through the slab along the symmetrical axis is equally divided into two beams. The above imaging and beam separation are irreversible.

Finally we mention that novel acoustic devices may be designed based on the proposed structures, e.g., superlens with or without deviated imaging function, beam splitters, sound shield, etc. The present parametric study in this paper for the negative refraction and imaging should be of help in optimizing the design of these acoustic devices.

Acknowledgements

The authors are grateful to the support from the National Natural Science Foundation of China under Grant number 11272041.

References

[1] V.G. Veselago, Sov. Phys. Usp. 10 (1968) 509.
[2] D.R. Smith, W.J. Padilla, D.C. View, S.C. Nemat-Nasser, S. Schultz, Phys. Rev. Lett. 84 (2000) 4184.
[3] R.A. Shelby, D.R. Smith, S. Schultz, Science 292 (2001) 77.
[4] J.B. Pendry, Phys. Rev. Lett. 85 (2000) 3966.
[5] P. Markos, C.M. Soukoulis, Phys. Rev. E 65 (2002) 036622;
P. Markos, C.M. Soukoulis, Phys. Rev. B 65 (2002) 033401.
[6] S. Foteinopoulou, E.N. Economou, C.M. Soukoulis, Phys. Rev. Lett. 90 (2003) 107402.
[7] A.A. Houck, J.B. Brock, I.L. Chuang, Phys. Rev. Lett. 90 (2003) 137401.
[8] E.J. Read, M. Soljacic, J.D. Joannopoulos, Phys. Rev. Lett. 91 (2003) 133901.
[9] C. Luo, M. Ibanescu, S.G. Johnson, J.D. Joannopoulos, Science 299 (2003) 368.
[10] C. Luo, S.G. Johnson, J.D. Joannopoulos, J.B. Pendry, Phys. Rev. B 65 (2002) 201104 (R);
C. Luo, S.G. Johnson, J.D. Joannopoulos, J.B. Pendry, Phys. Rev. B 68 (2003) 045115.
[11] E. Cubukcu, K. Aydin, E. Ozbay, S. Foteinopoulou, C.M. Soukoulis, Nature 423 (2003) 604.
[12] Y.Q. Ding, Z.Y. Liu, C.Y. Qiu, J. Shi, Phys. Rev. Lett. 99 (2007) 093904.
[13] G.W. Milton, New J. Phys. 9 (2007) 359.
[14] S. Zhang, L. Yin, N. Fang, Phys. Rev. Lett. 102 (2009) 194301.
[15] S.H. Lee, C.M. Park, Y.M. Seo, Z.G. Wang, C.K. Kim, Phys. Rev. Lett. 104 (2010) 054301.
[16] A. Sukhovich, L. Jing, J.H. Page, Phys. Rev. B 77 (2008) 014301.
[17] J.F. Robillard, J. Bucay, P.A. Deymier, A. Shelke, K. Muralidharan, B. Merheb, J.O. Vasseur, A. Sukhovich, J.H. Page, Phys. Rev. B 83 (2011) 224301.
[18] S.S. Peng, Z.J. He, H. Jia, A.Q. Zhang, C.Y. Qiu, M.Z. Ke, Z.Y. Liu, Appl. Phys. Lett. 96 (2010) 263502.
[19] K. Deng, Y.Q. Ding, Z.J. He, H.P. Zhao, J. Shi, Z.Y. Liu, J. Appl. Phys. 105 (2009) 124909.
[20] M. Ambati, N. Fang, C. Sun, X. Zhang, Phys. Rev. B 75 (2007) 195447.
[21] X.M. Zhou, M.B. Assouar, M. Oudich, Appl. Phys. Lett. 105 (2014) 233506.
[22] M.Z. Ke, Z.Y. Liu, C.Y. Qiu, W.G. Wang, J. Shi, W.J. Wen, P. Sheng, Phys. Rev. B 72 (2005) 064306.
[23] J. Li, Z.Y. Liu, C.Y. Qiu, Phys. Rev. B 73 (2006) 054302.
[24] J. Li, Z.Y. Liu, C.Y. Qiu, Phys. Lett. A 372 (2008) 3861–3867.
[25] C. Croënne, E.D. Manga, B. Morvan, A. Tinel, B. Dubus, J. Vasseur, Phys. Rev. B 83 (2011) 054301.
[26] B. Morvan, A. Tinel, J. Vasseur, B. Dubus, Appl. Phys. Lett. 96 (2010) 101905.
[27] C.Y. Chiang, P.G. Luan, J. Phys. Condens. Matter 22 (2010) 055405.
[28] A.C. Hladky-Hennion, J.O. Vasseur, G. Haw, Appl. Phys. Lett. 102 (2013) 144103.
[29] X.M. Zhou, M.B. Assouar, M. Oudich, J. Appl. Phys. 116 (2014) 194501.
[30] M. Addouche, M.A. Al-Lethawe, A. Choujaa, A. Khelif, Appl. Phys. Lett. 105 (2014) 023501.
[31] M.A. Al-Lethawe, M. Addouche, A. Khelif, S. Guenneau, New J. Phys. 14 (2012) 123030.
[32] A. Spadoni, M. Ruzzene, S. Gonella, F. Scarpa, Wave Motion 46 (2009) 435–450.
[33] R. Zhu, X.N. Liu, G.K. Hu, C.T. Sun, G.L. Huang, Nat. Commun. 5 (2014) 5510.
[34] Y.F. Wang, Y.S. Wang, Ch. Zhang, J. Phys. D, Appl. Phys. 47 (2014) 485102.
[35] Y. Achaoui, A. Khelif, S. Benchabane, V. Laude, J. Phys. D, Appl. Phys. 43 (2010) 185401.